

Soft X-ray spectroscopy of highly charged silicon ions in dense plasmas

G.Y. Liang¹, G. Zhao¹, and J.Y. Zhong^{1,2}

National Astronomical Observatories, Chinese Academy of Sciences

gzhao@bao.ac.cn

and

Y.T. Li², Y.Q. Liu², Q.L. Dong², X.H. Yuan², Z. Jin², and J. Zhang²

Institute of Physics, Chinese Academy of Sciences

jzhang@aphy.iphy.ac.cn

ABSTRACT

Rich soft X-ray emission lines of highly charged silicon ions (Si VI–Si XII) were observed by irradiating an ultra-intense laser pulse with width of 200 fs and energy of ~ 90 mJ on the solid silicon target. The high resolution spectra of highly charged silicon ions with full-width at half maximum (FWHM) of $\sim 0.3\text{--}0.4\text{\AA}$ is analyzed in wavelength range of 40–90 \AA . The wavelengths of 53 prominent lines are determined with statistical uncertainties being up to 0.005 \AA . Collisional-radiative models were constructed for Si VI – Si XII ions, which satisfactorily reproduces the experimental spectra, and helps the line identification. Calculations at different electron densities reveal that the spectra of dense plasmas are more complicate than the spectra of thin plasmas. A comparison with the Kelly database reveals a good agreement for most peak intensities, and differences for a few emission lines.

Subject headings: line: identification – methods: analytical –methods: laboratory

1. Introduction

Spectroscopic observations with the space-based observatories in soft X-ray and extreme-ultraviolet (EUV) regions provide valuable diagnostic means for understandings of the astrophysical hot plasma. The soft X-ray and EUV regions contain rich emission lines that can be used for determinations of plasma properties and element abundances over a wide temperature range (Mewe et al.

¹A20 Datun Road, Chaoyang District, Beijing 100012, China.

²P.O.Box 603, Beijing 100080, China.

2001; Ness et al. 2001, 2002a,b, 2003, etc.). The emissions are mainly from L-shell transitions of abundant astrophysical elements and M-shell transitions of iron ions. The most abundant element—Fe, shows a forest-like emission lines at the soft X-ray and EUV regions in the solar and stellar observations. So the spectral analyses of L-shell iron ions received strong attentions for astronomers and physicians. However, the emissions lines mainly span $6\text{--}18 \text{ \AA}$ ($\Delta n \geq 1$, here n is main quantum number) and $100\text{--}350 \text{ \AA}$ ($\Delta n = 0$) regions. So previous space observatories, e.g. *Skylab* (covering $6\text{--}49 \text{ \AA}$), Solar EUV Rocket Telescope and Spectrograph (SERTS, $170\text{--}450 \text{ \AA}$), Extreme Ultraviolet Explore (*EUVE*, covering $70\text{--}760 \text{ \AA}$ with a resolution of $\Delta\lambda=0.4\text{--}2.5 \text{ \AA}$) (Brickhouse et al. 2000), and Solar Ultraviolet Measurements of Emitted Radiation (SUMER, covering $500\text{--}1610 \text{ \AA}$ with resolution power of $\lambda/\Delta\lambda = 19000\text{--}40000$) instrument on SOHO mission etc., probe into the universe in the two wavelength ranges. However, the spectra between $40\text{--}90 \text{ \AA}$ has received a scant attention even in solar measurements. Though the new generation of space mission of *Chandra X-ray Observatory* covers wavelength range of $1.2\text{--}176 \text{ \AA}$ with higher resolution of $\sim 0.06 \text{ \AA}$ (Brinkman et al. 2000; Mewe et al. 2001; Ness et al. 2002b; Argiroff et al. 2003), most researches focus on observations below $\sim 35 \text{ \AA}$ provided by High Energy Transmission Grating Spectrometer (HETGS) (with $\Delta\lambda=0.012$ and 0.023 \AA) on *Chandra* and Reflected Grating Spectrometer (RGS) (with $\Delta\lambda=0.05 \text{ \AA}$) on *XMM-Newton* (Canizares et al. 2000; Audard et al. 2001; Brinkman et al. 2001). This is due to the spectral region is spanned by $\Delta n \geq 1$ transition lines of highly charge iron ions.

The region of $40\text{--}90 \text{ \AA}$ contains more lines than currently identified, as graphically illustrated by *Chandra* spectra of Capella (Brinkman et al. 2000) and Procyon (Raassen et al. 2002) observed with Low Energy Transmission Grating Spectrometer (LETGS). Those unresolvable weak lines form the pseudo-continuum emissions, and raise the “background” level for strong features, and increase the uncertainty to their interpretation. Contribution to these unidentified lines may come from L-shell ions of magnesium, silicon, sulfur, argon, calcium, iron and nickel. Nevertheless, the uncertainties of wavelength and cross section of excitation, ionization and recombination are more significant for L-shell ions than K-shell ions of above listed elements. The associated uncertainties greatly impede our efforts to fully understand astrophysical X-ray sources, such as the shape of emission measure distribution, element abundances, and spatial structures. So laboratory studies, using, for example, electron-beam ion traps (EBIT), storage rings, tokamaks, and intense laser pulses, are very necessary to provide accurate atomic data that can be incorporated into astrophysical spectral synthesis codes.

The interaction of intense, sub-picosecond laser pulses with solid targets allows the generation of hot plasmas with a temperature between 50 eV and 1 keV , which is the typical temperature range of stellar coronae, and a density of $10^{19}\text{--}10^{21} \text{ cm}^{-3}$. The laser plasma is one of ground X-ray and EUV sources. This type plasma plays an important role in various fields of research such as astrophysics, inertial confinement fusion, etc (Lindl et al. 2004). Its X-ray and EUV radiation can be used to determine plasma conditions and micro-processes. For example the density can be obtained from line broadening effects, and the temperature can be estimated from satellites of H-like Ly α and He-like resonance ($1s2p \ ^1P_1\text{--}1s^2 \ ^1S_0$) lines. The well controlled laser plasma can

also be used to benchmark the kinetic codes (Glenzer et al. 2000), and simulate some astrophysical phenomena.

Recently, many efforts have been made in laboratories to provide accurate atomic data and validate the simulation codes. Glenzer et al. (2000) and other groups (Skobelev et al. 1997; Biedermann et al. 2002) investigated the X-ray emissions of K-shell ions of argon, using the intense pulsed laser, electron beam ion traps (EBIT) and tokamaks. Independent methods such as Thomson Scattering and infrared interferometer measurement for temperature and density, have been used to benchmark the T_e and n_e constrained by spectroscopy, and a good agreement is obtained. Lepson et al. (2003, 2005) further investigated the soft X-ray emissions of L-shell ions of argon (20–50 Å) and sulfur (20–75 Å) using the Lawrence Livermore EBIT-I and EBIT-II, and graphically illustrated larger uncertainties in available atomic data. Yang et al. (2000) measured emissions of sulfur in wavelength range of 190–400 Å by beam-foil spectroscopy in the Heavy Ion Research Facility at Lanzhou.

In this paper, the experimental setup and the calibration for the soft X-ray and EUV spectrometer are described in Sect. 2. Results and discussions are presented in Sect. 3. In this section, the soft X-ray spectra of highly charged silicon ions, modelling to the spectra, and the comparison between the present calculation and the Kelly database are described in detail. Finally, the conclusions is outlined in Sect. 4.

2. Experimental setup and spectrometer calibration

The experiment was carried out using the Xtreme Light II (XL-II) laser system at the Institute of Physics (IoP), Chinese Academy of Sciences (Peng et al. 2004, Li et al. 2006). The laser system has an output energy up to 650mJ in 30fs pulses at 796 nm. The laser beam was focused by an $f/5$ lens to a dimension of $\sim 26 \times 24 \mu\text{m}$ on the surface of a planner target, which is consist of three materials including copper, plastic and silicon as shown by the left-top panel of Fig. 1. The copper is used for collimation, while the plastic is used for wavelength calibration in the selected wavelength range. A grazing-incidence flat field grating spectrometer with varied spacing grating (average groove density is 1200 l/mm), was adopted to disperse the radiation. A cooled CCD camera (running at -24 °C) is used for readout of the spectrograph. The CCD chip has 2048×512 pixels with each of $\sim 13.5 \times 13.5 \mu\text{m}^2$ and thus, the CCD total surface area is about $28 \times 7 \text{ mm}^2$. The detail description refers to the work of Liu et al. (2004). The spectrometer can cover soft X-ray and Extreme Ultraviolet (EUV) region (40–400 Å) by sliding the CCD camera along the dispersion plane. In the present single setting, the wavelength coverage is 40–180 Å, which is the shortest wavelength range covered by the designed spectrometer. The spectral resolution is about $\delta\lambda \sim 0.3$ over 40–90 Å.

Figure 1 shows the experimental layout. The laser beam with energy of 90 mJ and pulse duration of 200 fs was focused onto the target in direction of 45° to the target normal, with

intensity of $\sim 10^{15}$ W/cm². Firstly, the focused laser irradiates the plastic. As shown by the CCD spectral image in Fig.1, there is a slight rotation between pixel rows and the dispersion direction. A program is compiled to correct this rotational misalignment before summing over the pixel channels. Additionally, a clear discrete band is observed in direction being perpendicular to the grating dispersion. This is due to the toroidal mirror placed before the entrance slit. So the spectra in pixel region of 60–260 is selected in summing over the pixel channels.

In order to obtain the dispersion function of the present spectrometer, 14 well-known lines from highly charged carbon, nitrogen and oxygen ions, and their higher order diffraction covering the whole wavelength range of interest are used, as shown by symbols in Fig. 2. Peak centroids of these emission lines are determined through Gaussian fit, which can describe the observed line shape satisfactorily as shown by the inset in Fig. 2. A full-width at half maximum (FWHM) of $\sim 3.5\text{--}4.5$ pixels is found, corresponding to $\delta\lambda \sim 0.3\text{--}0.4$ Å. The measured line width ($\sim 3.5 \times 13.5 = 47$ μm, with each pixel size of 13.5 μm) reflects the width of entrance slit of 50 μm. The wavelength values of the calibration lines were adopted from NIST database¹ and the website <http://www.pa.uky.edu/~peter/atomic/>. A parabolic polynomial is used to represent the pixel (x)-wavelength (λ) relation [see Fig. 2]. The calibration uncertainty is estimated to be 0.11 Å [rms value] over the range of 40–180 Å. Multi-measurements and calibrations reveal that the calibration parameters hold constant.

3. Results and discussions

3.1. Soft X-ray spectrum of highly charge silicon

When the focused laser irradiate on the solid target, rich emission lines are observed, as shown in below image of Fig. 1. In this work, we pay special attention on the soft X-ray emission spectra in the wavelength range of 40–90 Å, as labelled out by white region in Fig. 1. 10 separate measurements were performed with each measurement of 4 continuous laser pulses irradiating on the target and 30 s accumulation. Using the calibration parameters, we scale all the measurements. Fig. 3 illustrates the averaged spectrum and its best-fitting in wavelength range of 40–90 Å. In this region, emission lines are dominated by $\Delta n \geq 1$ transition lines of Si VI–Si XII ions.

We separately analyze the 10 spectra, and accurately determine the wavelengths for 53 prominent lines. A statistical accuracy of 0.005 Å is obtained for those strong and blend-free lines, as listed in the second column of Table 1.

Based upon the theoretical wavelengths and relative line intensities [explained in the next subsection], we identified these emission lines. The identified wavelength values are partially from

¹<http://physics.nist.gov/PhysRefData/ASD/index.html>

our recent calculations (Liang et al. 2007), NIST database² and Kelly database³ (Kelly 1987). In the third subsection, the detailed comparison of the present calculation and the Kelly database is given. From Table 1, the differences between the measurements and available database are within 0.1 Å for most emission lines, whereas differences up to 0.3 Å also appears for some emission lines. This reveals that detailed structure calculations for L-shell silicon ions by inclusion of large configuration interactions and relativistic effects are necessary.

3.2. Modelling

In soft X-ray region, forest-like lines from L-shell ions generally group together or blend each other when the broadening from spectrometers has been considered, as in this case. Besides, large discrepancies of line wavelengths between measurements and calculations have been demonstrated for highly charged sulfur (~ 0.3 Å) and argon (~ 0.1 Å) ions. So the predictions of line intensities are necessary for the line identification.

Collisional-radiative (CR) models for highly charged Si VI–Si XII ions are constructed to simulate the experimental spectrum. The atomic data used to calculate the line intensities, are generated with the Flexible Atomic Code (FAC) provided by Gu (2003). A fully relativistic approach based on Dirac equation is used throughout the entire package. Energy levels, transition rates of E1, E2, M1, and M2 types, and electron impact excitation strengths have been reevaluated for Si IX–Si XI in our recent work (Liang et al. 2007). 782, 878, 312, 560, 320, 350 and 40 energy levels, have been included in predictions of line intensities for Si VI–Si XII, respectively. These levels belongs to not only singly excited configurations, but also some doubly excited configurations for accounting for configuration interaction effect as fully as possible. All possible $\Delta n = 0$ (2–2) and $\Delta n > 0$ (2–3, 2–4, and 2–5) decay rates, excitations and de-excitations among levels mentioned above have been considered in the present simulation work.

The theoretical spectra have been computed in the steady state equilibrium. The set of CR equations are solved by normalizing the total level populations of each charge state to 1. The theoretical spectrum for each charge stage is calculated at a density of $1.0 \times 10^{20} \text{ cm}^{-3}$ and temperatures of maximum fraction in ionization equilibrium of Mazzotta et al. (1998). The calculated line intensities are fold by Gaussian profile with FWHM of 0.3 Å being comparable to the experimental resolution. The theoretical spectra are normalized by the measured values at 80.353 Å, 71.425 Å, 62.052 Å, 55.569 Å, 50.278 Å, 47.670 Å and 44.135 Å for Si VI–Si XII, respectively. As shown in Fig. 4, the simulation satisfactorily reproduces the experimental spectra of highly charged silicon ions. Different color curves indicate the spectra of different charge states. By the comparison, most prominent emission lines are identified as given in Table 1.

²<http://physics.nist.gov/PhysRefData/ASD/index.html>

³<http://cfa-www.harvard.edu/amp/ampdata/kelly/kelly.html>

Since the broadening from the entrance slit, the measured line width is about 0.3–0.4 Å. Many emission lines of L-shell ions grouped together, as illustrated by the spectra of Si XI (dashed and/or dotted curves) in Fig. 5-(a), so that the line identification is very difficult. In thus case, we usually assign the largest contribution to the emission peak. For example, we assign the peaks at 46.403 and 47.670 Å to the $2s3d\ ^3D_2$ – $2s2p\ ^3P_2$ (46.399 Å) and $2p3d\ ^3D_3$ – $2p^2\ ^3P_2$ (47.653 Å) transitions of Si XI, respectively.

It should be noted that at the density of the laser plasma, more than half an ion's total level population can be in excited levels, and even in doubly excited levels, other than the ground level. So many lines excited from lowest lying excited levels can be observed, e.g. lines at 46.403 Å of Si XI, 49.828 Å of Si X, 55.950 Å of Si IX etc. Due to the high-density effect, the spectra of laser plasma is more complicate than the spectra in low density plasmas such as the astrophysical, electron beam ion trap, and tokamak plasmas. In Fig. 5-(b), we show the spectrum of Si XI at high ($1.0 \times 10^{20} \text{ cm}^{-3}$, blue-solid curve) and low ($1.0 \times 10^{10} \text{ cm}^{-3}$, red-solid curve) electron densities. The emission line intensities around 47.67 Å are greatly suppressed, whereas the line intensities around 46.403 Å are enhanced at the low-density plasma. This is due to that the emission lines around 47.67 Å are from higher excited level of $2p^2$ configuration. In case of the low-density plasma, the level population is mainly in the ground level.

3.3. Comparison between present calculation and Kelly database

Based upon the normalization for each charge states [see caption of Fig. 4], we compare present spectra with the results from Kelly database (Kelly 1987). For lines at 46.403 and 49.343 Å of Si XI, present calculation shows a better agreement with the measurement [see Fig. 4]. Moreover, Kelly predicted a stronger Si XI line at 50.517 Å than the present calculation, which blends with an emission line at 50.278 Å of Si X. By multi-Gaussian component fitting, contribution from the two features can be estimated in the measurement at the peak position of 50.50 Å as listed in Table 1. The blending results into two peaks around 50.5 Å in the sum spectrum [see Fig. 6] of Kelly. Another strong Si XI line at 52.296 Å is predicted in Kelly work, which helps our identification for the peak at 52.291 Å in the measurement. However, this emission line is missed in our calculation.

For peak at 51.796 Å, present calculation is higher than the measurement by 30%, whereas Kelly database misses lines at this peak position. For the peak at 53.736 Å, the two predictions agree with each other, and well agree with the measurements [see Fig. 4]. Kelly predicts a strong line at 54.599 Å of Si X, which is two times of the present prediction. The present value is comparable with the measured intensity at 54.705 Å. So we assign the emission line to Si X (54.599 Å).

For peak around 55.034, 55.379, 55.567, and 55.950 Å, present calculation predicts 4 Si IX lines with intensities being agreement with the measurement. Contributions from a group weak Si X lines (around 55.969 Å) compensates the difference between experiment and prediction of Si IX at the peak of 55.950 Å. Kelly database further predicts a Si X line (55.096 Å) at the peak

of 55.034 Å, which results a large deviation at the peak at 55.034 Å. For the peak at 55.567 and 55.950 Å, Kelly's values are lower than the measurement by ~40%, and no other weak blending. For the peak at 59.088 Å Kelly and this work predict a strong line at 59.004 Å. Another important contribution from Si IX line at 58.906 Å is estimated in this work, whereas Kelly predicts another line of Si VIII (58.885 Å) being higher than present value by factors. The two work predict a strong Si VII line close to the peak position (59.088 Å), which results into the large difference between the sum spectra and the measurement at this wavelength [see Fig. 6].

For the peaks at 61.256 and 62.052 Å, Kelly and present works predict two Si VIII lines (see Table 1) with intensities being agreement with the measurements [see Fig. 4]. However, Kelly further shows a considerable contribution from Si X and Si VII at the peak of 61.256 Å, which results into the sum intensity is higher than the experiment value by ~60%. For peaks at 62.993, 63.377, 63.762, and 64.482 Å, Kelly's predictions show a better agreement with the measurement than the present calculation. Whereas, the peak intensities at 65.977 and 67.418 Å are satisfactorily reproduced in the present work, yet Kelly misses the contribution around 65.977 Å and overestimates the contribution around 67.418 Å and 72.389 Å by a factor up to ~1.0.

For the peaks at 68.294, 69.734, 70.129, and 71.953 Å, the two calculations predict line intensities of Si VII being consistent with the measurements [see Fig. 4]. However, considerable contribution from Si VIII ($69.790 \text{ Å } 2s^2 2p^2(^3p)3s\ ^4P_{3/2} - 2s^2 2p^3\ ^4S_{3/2}$) is predicted in Kelly database, which results into the sum intensity is greatly higher than the measured value. For the peaks at 73.136, 73.394 and 75.160 Å, the two works satisfactorily reproduce the measurement, whereas a considerable contribution from Si VI is estimated in Kelly database at 75.160 Å. For the peaks 79.132, 79.448, 81.382, 81.698 and 83.809 Å, present calculation underestimates the contribution from Si VII, however Kelly database overestimates the contribution. Additionally, Kelly database satisfactorily reproduce the peak at 84.935 and 85.330 Å with wavelength higher than the measurement by ~0.28 Å. But present prediction greatly underestimate the line intensities. Around the peak at 88.0 Å, one strong emission line with wavelength of 87.641 and 88.008 Å is predicted by present model and the Kelly database, and the Kelly database shows a better agreement with the measured value. The partially blended emission line is from the second order diffraction of the Si XII line at 44.165 Å.

For the emission lines of Si VI ions, Kelly's result shows a good agreement with the measurement at 77.348 and 77.626 Å, and better than the present prediction. For the peaks at 83.328 and 83.808 Å, our results agree with the Kelly predictions, whereas they are lower than the measured values by ~30%–90%.

4. Conclusions

Soft X-ray spectroscopy of highly charged silicon has been measured with the flat-field grating spectrometer mounted on one observation port of the Xtreme Light II at the Institute of Physics,

Chinese Academy of Sciences. The observed line-width is $\sim 0.3\text{--}0.4 \text{ \AA}$ over the wavelength range of $40\text{--}180 \text{ \AA}$, which is due to the broadening from entrance slit with width of $50 \mu\text{m}$. Using well-known lines of highly charged carbon, nitrogen and oxygen, the dispersion function of the spectrometer is calibrated with calibration uncertainty of 0.11 \AA over the wavelength range of $40\text{--}180 \text{ \AA}$. In multi-measurements, 53 prominent lines are reproduced and their wavelengths are determined with accuracy of $0.11\text{--}0.15 \text{ \AA}$ (including statistical uncertainty listed in Table 1, and the calibration uncertainty of 0.1 \AA).

Collisional-radiative models has been constructed for each charge states which satisfactorily reproduce the measurements. With the aid of the simulation, we identified the 53 prominent lines. The wavelength differences between present calculations and measurements is within 0.1 \AA for most lines. In some case, the differences can be up to 0.3 \AA , which reveals the detailed atomic structure calculation with inclusion of large configuration interaction and relativistic effects, is necessary.

Calculations at different electron densities, indicate that the spectra of the dense plasma are more complicate than the spectra from thin plasmas such as astrophysical, electron beam ion trap and tokamak plasmas. This is due to that the high density effect results into the higher level population in the excited levels than in cases of the low-density plasmas.

A comparison with the Kelly database is also performed, which reveals a good agreement for most peaks, and differences for some peak intensities, such as at 71.953 , 77.348 , 81.698 , 83.809 , and 87.629 \AA . Similarly, the two predictions are benchmark by comparing with the measurements. The presence of discrepancies also leave a scope to investigate the density effect in the high-dense plasma.

This work was supported by the National Natural Science Foundation of China under Grant No. 10603007, 10510490, and 10521001, as well as National Basic Research Program of China (973 Program) under grant No. 2007CB815103.

REFERENCES

- Argiroffi, C., Maggio, A., & Peres, G. 2003, *A&A*, 404, 1033
- Audard, M., Behar, E., Güdel, M., et al. 2001, *A&A*, 365, L329
- Brickhouse, B.S., Dupree, A.K., Edgar, R.J., Liedahl, D.A., Drake, S.A., White, N.E., & Singh, K.P. 2000, *ApJ*, 530, 387
- Biedermann, C., Radtke, R., & Fournier, K.B. 2002, *Phys. Rev. E*, 66, 066404
- Brinkman, A.C., Behar, E., Güdel, M., et al. 2001, *A&A*, 365, L324
- Brinkman, A.C., Gunsing, C.J.T., Kaastra, J.S., et al. 2000, *ApJ*, 530, L111

- Canizares, C.R., Huenemoerder, D.P., Davis, D.S., et al. 2000, ApJ, 539, L41
- Glenzer, S.H., Fournier, K.B., Decker, C., et al. 2000, Phys. Rev. E, 62, 2728
- Gu, M.F. 2003, ApJ, 590, 1131
- Kelly, R.L. 1987, J.Phys.Chem.Ref.Data, 16, Suppl. 1.
- Lepson, J.K., Beiersdorfer, P., Behar, E., & Kahn, S.M. 2003, ApJ, 590, 604
- Lepson, J.K., Beiersdorfer, P., Behar, E., & Kahn, S.M. 2005, ApJ, 625, 1045
- Li, Y.T., Yuan, X.H., Xu, M.H., et al. 2006, Phys.Rev.Lett., 96, 165003
- Lindl, J.D., et al. 2004, Phys. Plasmas, 11, 339
- Liang, G.Y., Zhao, G., & Zeng, J.L. 2007, Atom. Data and Nucl. Data Tables, (in press)
- Liu, Y.Q., Zhang, J., Chen, Z.L., & Peng, X.Y. 2004, Acta Phys. Sinica, 53, 1433
- Mazzotta, P., Mazzitelli, G., Colafrancesco, S., & Vittorio, N. 1998, A &AS, 133, 403
- Mewe, R., Raassen, A.J.J., Drake, J.J., Kaastra, J.S., van der Meer, R.L.J., & Porquet, D. 2001, A&A, 368, 888
- Ness, J.-U., Brickhouse, N.S., Drake, J.J., & Huenemoerder, D.P. 2003, ApJ, 598, 1277
- Ness, J.-U., Mewe, R., Schmitt, J.H.M.M., et al. 2001, A&A, 367, 282
- Ness, J.-U., Schmitt, J.H.M.M., Burwitz, V., Mewe, R., Rassen, A.J.J., van der Meer, R.L.J., Predehl, P., & Brinkmann, A.C. 2002a, A&A 394, 911
- Ness, J.-U., Schmitt, J.H.M.M., Burwitz, V., Mewe, R., & Predehl, P. 2002, A&A, 387, 1032
- Peng, X.Y., Zhang, J., Jin, Z., et al. 2004, Phys.Rev.E, 69, 026414
- Raassen, A.J.J., Mewe, R., Audard, M., et al. 2002, A&A, 389, 228
- Skobelev, I.Y., Faenov, A.Y., & Dyakin, V.M. 1997, Phys. Rev. E, 55, 3773
- Yang, Z.H., Ma, X.W., Wang, Y.D., Liu, P.H., & Yu, Y.D. 2000, ApJ, 544, 572

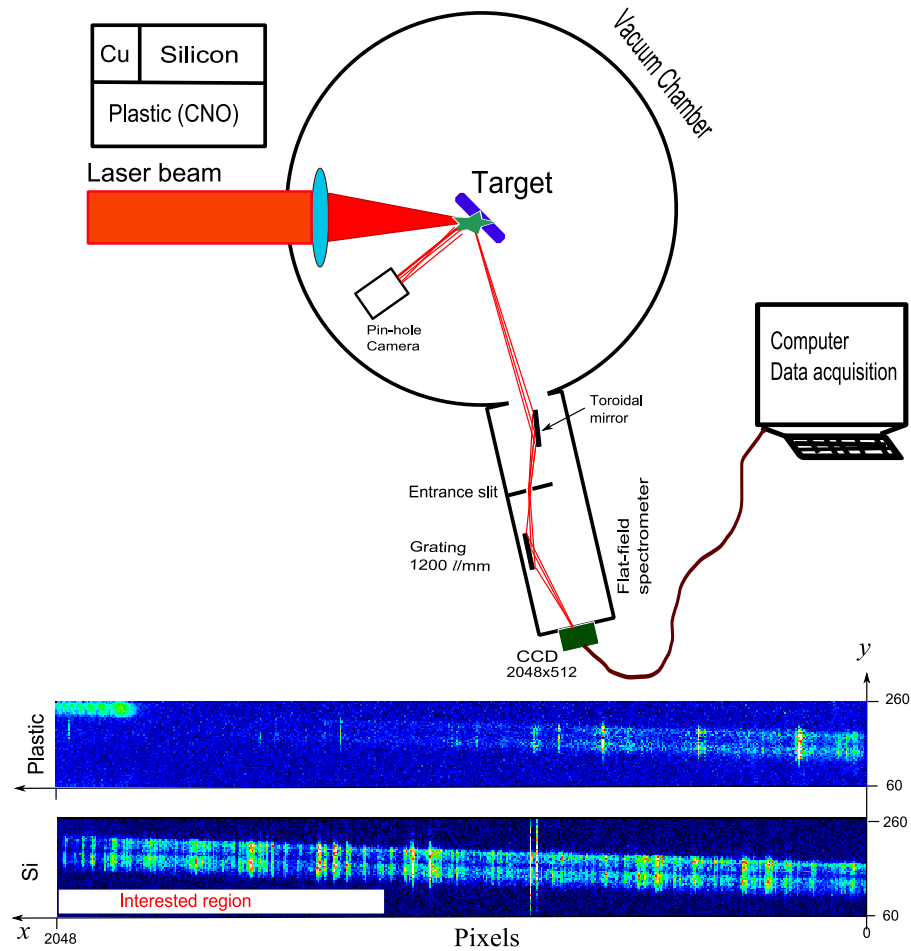


Fig. 1.— (Online color) The schematic diagram of the experimental setup. The left-top panel is the target configuration. The bottom panel is partial readout image (60–260 pixel region in direction of perpendicular to dispersion direction) of the CCD camera. The interest region of this work is denoted by the white stray.

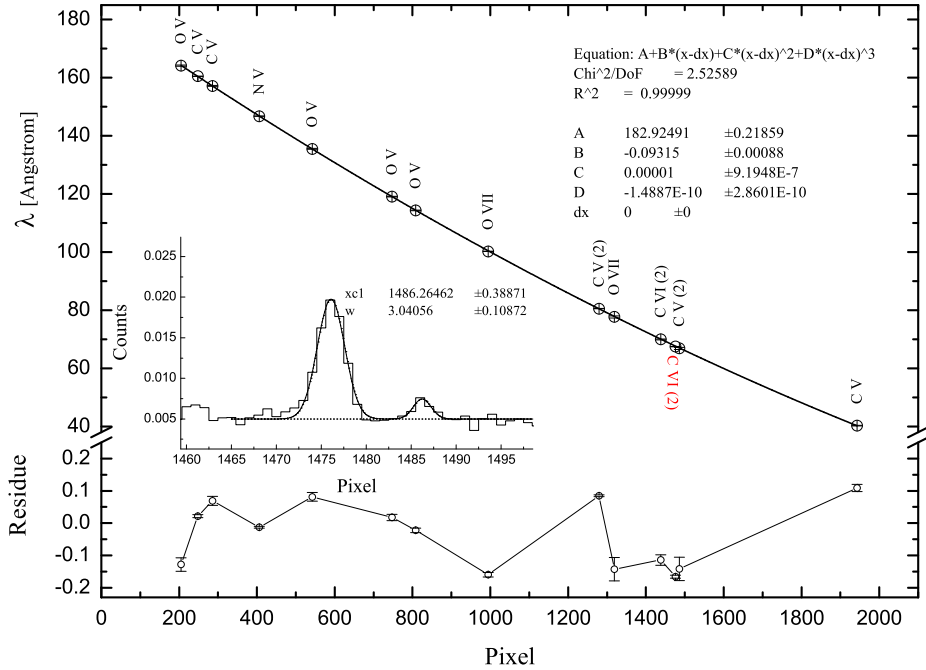


Fig. 2.— (Online color) Dispersion function of the flat-field soft X-ray/EUV spectrometer obtained from a cubic polynomial fit and its residue (bottom) in wavelength range of 40–180 Å. Symbols with error bars are calibration lines and their residues. The inset spectrum shows a calibration line used and its fit with Gaussian profile, which is marked by red “C VI (2)” around dispersion curve.

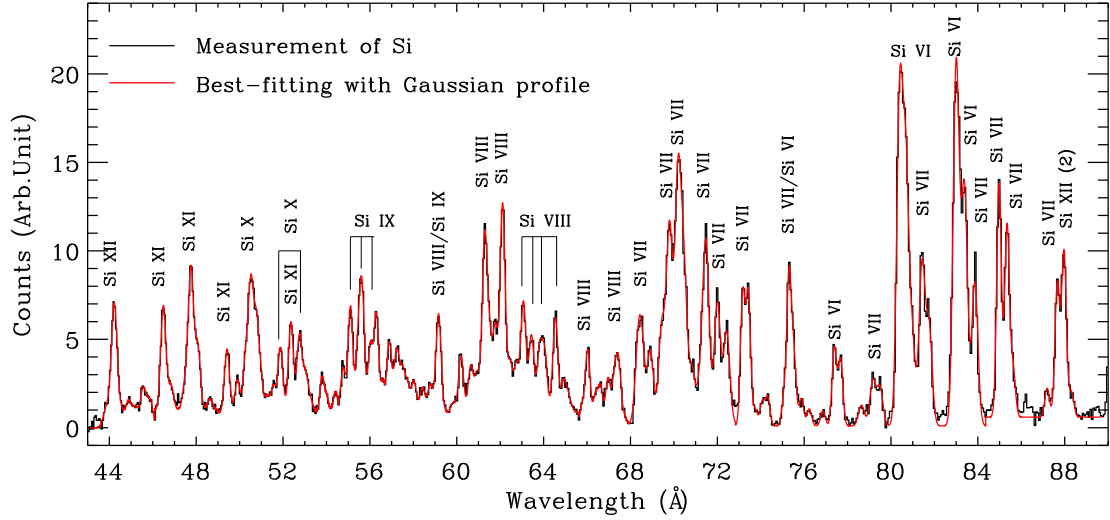


Fig. 3.— (Online color) Averaged spectrum (black histogram) of 10 measurements of highly charged silicon ions produced by Xtrem Light II laser system (with a pulse duration of ~ 200 fs and an energy of ~ 90 mJ) at the IoP, and its best-fitting (red) in range of 40–90 Å. For prominent lines, identifications are labelled out.

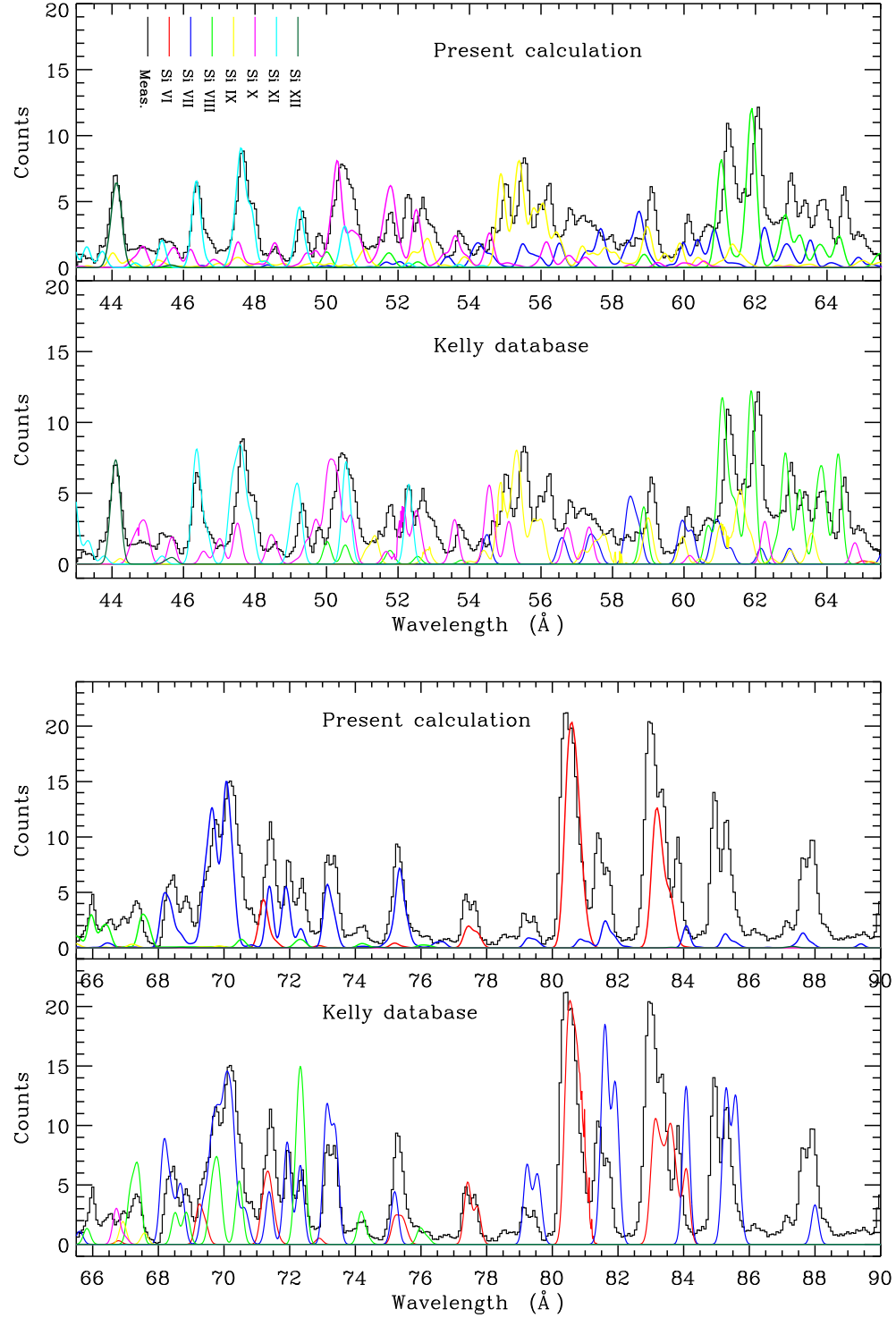


Fig. 4.— (Online color) Experimental (histogram curve) and synthesized spectra (color) of highly charged silicon ions at a density of $1.0 \times 10^{20} \text{ cm}^{-3}$. The calculations are normalized to the measured ones according to lines at 80.353 \AA , 71.425 \AA , 62.052 \AA , 55.569 \AA , 50.278 \AA , 47.670 \AA and 44.135 \AA for Si VI–Si XII, respectively.

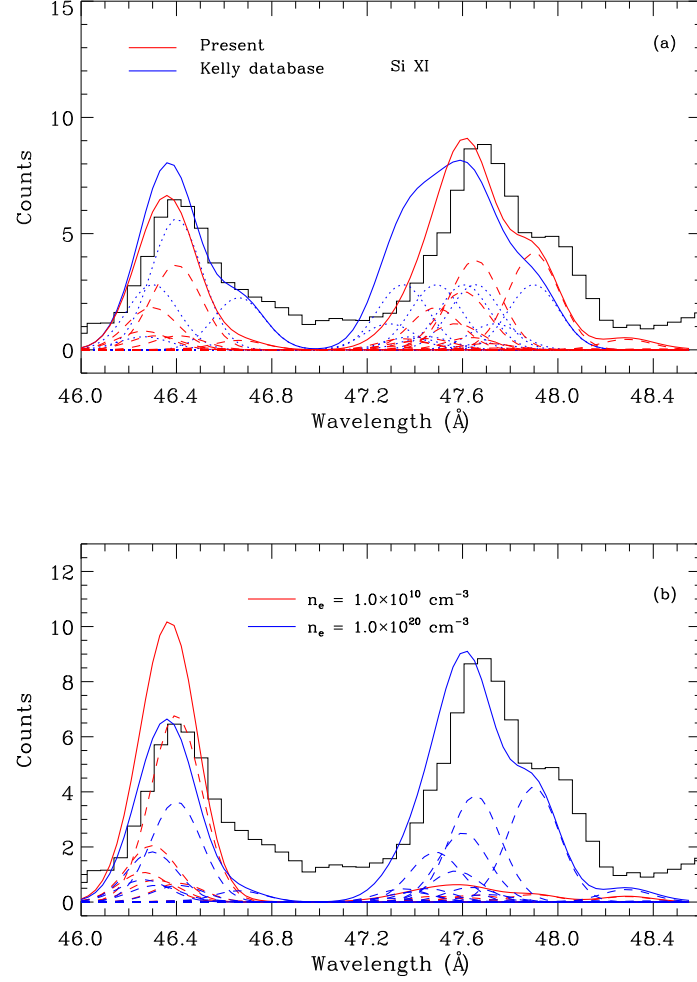


Fig. 5.— (Online color) Emission lines of highly charged Si XI in range of 46–48.6 Å. The theoretical line intensities are folded by Gaussian profile with FWHM 0.3 Å. (a) Present calculated spectra of Si XI (red-solid line added from red-dashed lines for individual emissions of Si XI), and the spectra derived from Kelly database (blue-solid line added from blue-dotted lines for individual emissions of Si XI). The theoretical spectra are normalized by the experimental peak at 47.67 Å. (b) Present calculation for thin ($1.0 \times 10^{10} \text{ cm}^{-3}$, red-solid line added from red-dashed lines for individual emissions of Si XI) and dense ($1.0 \times 10^{20} \text{ cm}^{-3}$, blue-solid line added from blue-dashed lines for individual emissions of Si XI) plasmas.

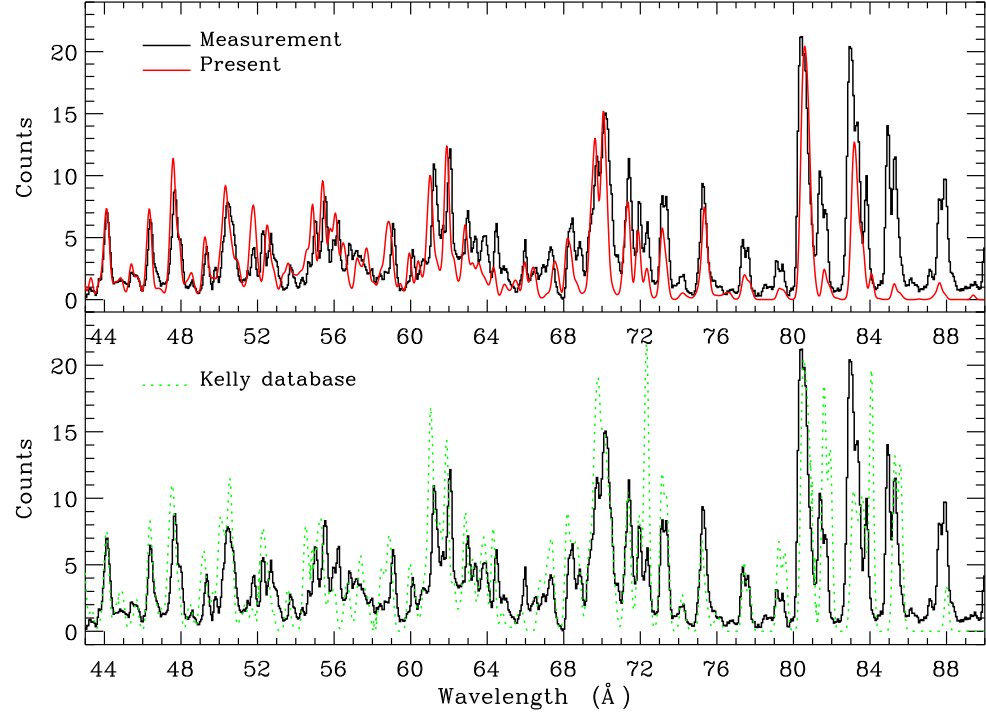


Fig. 6.— (Online color) Experimental and theoretical spectra of highly charged silicon ions in wavelength range of 43–90 Å. Based upon the normalization [see caption in Fig. 4], the sum of each charge state is shown by color curves for present calculation (red-solid) and Kelly database (green-dotted).

Table 1. Experimental wavelengths along with statistical errors of 53 prominent emission lines in wavelength range of 40–90 Å, and their identifications. The same number with different subscripts (in the Index column) denotes the blending lines.

Index	λ_{Exp} Å	Intensity Arb. Unit	λ_{Kelly} Å	$\Delta\lambda$ Å	Ion	$\lambda_{\text{Pres.}}$ Å	$\Delta\lambda$ Å	Ion	Transition			
									Upper		Lower	
1	44.143±0.008	10.73±0.52	44.165	-0.030	Si XII	44.165	-0.022	Si XII	2s ² 3d	² D _{5/2}	2s ² 2p	² P _{3/2}
2a	45.440±0.038	3.31 ±0.27				45.398	0.042	Si XI	2p3p	¹ D ₂	2s2p	¹ P ₁
2b	45.723±0.038	2.25 ±0.28	45.684	0.039	Si X	45.756	-0.033	Si X	2p ² (¹ D)3p	² P _{3/2}	2s2p ²	² D _{5/2}
3	46.403±0.004	7.86 ±0.21	46.401	0.002	Si XI	46.399	0.004	Si XI	2s3d	³ D ₂	2s2p	³ P ₂
4	47.670±0.006	10.52±0.33	47.653	0.017	Si XI	47.653	0.017	Si XI	2p3d	³ D ₃	2p ²	³ P ₂
5	47.989±0.008	4.78 ±0.21	47.899	0.090	Si XI	47.899	0.090	Si XI	2p3d	¹ F ₃	2p ²	¹ D ₂
6	49.343±0.005	4.49 ±0.16	49.222	0.121	Si XI	49.222	0.121	Si XI	2s3d	¹ D ₂	2s2p	¹ P ₁
7	49.828±0.011	2.29 ±0.15	49.701	0.127	Si X				2s2p(¹ P)3d	² F _{7/2}	2s2p ²	² D _{5/2}
8a	50.278±0.033	3.91 ±0.36	50.333	-0.055	Si X	50.333	-0.055	Si X	2s2p(³ P)3d	⁴ D _{7/2}	2s2p ²	⁴ P _{5/2}
8b	50.517±0.033	8.63 ±0.39	50.524	-0.007	Si XI				2p3s	³ P ₂	2p ²	³ P ₂
9	51.796±0.008	4.48 ±0.21				51.821	-0.045	Si X	2p ² (¹ D)3d	² F _{7/2}	2p ³	² D _{5/2}
10a	52.291±0.004	6.27±0.19	52.155	0.136	Si X				2s2p(¹ P)3d	² D _{5/2}	2s2p ²	² P _{3/2}
10b			52.296	-0.005	Si XI				2s3s	¹ S ₀	2s2p	¹ P ₁
11	52.687±0.009	5.33 ±0.28	52.485	0.202	Si X	52.484	0.203	Si X	2s2p(³ P)3d	² F _{7/2}	2s2p ²	² D _{5/2}
12a	53.736±0.010	1.94 ±0.17	53.573	0.163	Si X	53.572	0.164	Si X	2s2p(³ P)3d	² D _{5/2}	2s2p ²	² D _{3/2}
12b			53.595	0.141	Si X	53.596		Si X	2s2p(³ P)3d	² D _{3/2}	2s2p ²	² D _{3/2}
13	54.705±0.011	2.30 ±0.19	54.599	0.106	Si X	54.599	0.106	Si X	2s2p(³ P)3d	² P _{3/2}	2s2p ²	² S _{1/2}
14	55.034±0.004	6.19 ±0.20	54.907	0.127	Si IX	54.921	0.113	Si IX	2s2p ² (⁴ P)3d	⁵ D ₃	2s2p ³	⁵ S ₂
15	55.379±0.017	3.85 ±0.63	55.272	0.107	Si IX	55.272	0.107	Si IX	2s ² 2p3d	³ P ₂	2s ² 2p ²	³ P ₂
16	55.569±0.010	6.71 ±0.63	55.401	0.168	Si IX	55.401	0.168	Si IX	2s ² 2p3d	³ D ₃	2s ² 2p ²	³ P ₂
17	55.950±0.009	3.78 ±0.21	55.781	0.169	Si IX	55.779	0.171	Si IX	2s2p(⁴ P)3d	⁵ D ₃	2s2p ³	⁵ S ₂
18	56.229±0.006	5.69 ±0.22	56.027	0.202	Si IX	56.027	0.202	Si IX	2s ² 2p3d	¹ F ₃	2s ² 2p ²	¹ D ₂
19a	59.088±0.003	6.74 ±0.16				58.906	0.182	Si IX	2s2p ² (⁴ P)3d	³ F ₄	2s2p ³	³ D ₃
19b			59.004	0.084	Si IX	59.004	0.084	Si IX	2s2p ² (⁴ P)3d	³ F ₃	2s2p ³	³ D ₂

Table 1—Continued

Index	λ_{Exp} Å	Intensity Arb. Unit	λ_{Kelly} Å	$\Delta\lambda$ Å	Ion	$\lambda_{\text{Pres.}}$ Å	$\Delta\lambda$ Å	Ion	Transition			
									Upper		Lower	
19c			58.885	0.203	Si VIII				$2s^2p^3(^5S)3p$	${}^4P_{5/2}$	$2s^22p^3$	${}^4S_{3/2}$
20	61.256 ± 0.006	11.35 ± 0.49	61.070	0.186	Si VIII	61.032	0.224	Si VIII	$2s^22p^2(^1D)3d$	${}^2F_{5/2}$	$2s^22p^3$	${}^4S_{3/2}$
21	62.052 ± 0.004	14.88 ± 0.33	61.914	0.138	Si VIII	61.792	0.260	Si VIII	$2s^22p^2(^1D)3d$	${}^2F_{7/2}$	$2s^22p^3$	${}^2D_{5/2}$
22	62.993 ± 0.008	7.66 ± 0.33	62.849	0.144	Si VIII	62.849	0.144	Si VIII	$2s^22p^2(^3P)4s$	${}^2P_{1/2}$	$2s2p^4$	${}^4P_{5/2}$
23	63.377 ± 0.011	5.24 ± 0.29	63.229	0.148	Si VIII	63.241	0.136	Si VIII	$2s2p^3(^3S)3p$	${}^4P_{1/2}$	$2s2p^4$	${}^4P_{5/2}$
24	63.762 ± 0.012	4.23 ± 0.33	63.732	0.030	Si VIII	63.722	0.040	Si VIII	$2s^22p^2(^3P)3p$	${}^4P_{1/2}$	$2s^22p^3$	${}^2D_{5/2}$
25	64.482 ± 0.007	6.60 ± 0.27	64.327	0.155	Si VIII	64.317	0.165	Si VIII	$2s^22p^2(^3P)3d$	${}^2D_{5/2}$	$2s^22p^3$	${}^2P_{3/2}$
26	65.977 ± 0.007	4.48 ± 0.25	65.833	0.144	Si VIII	65.969	0.008	Si VIII	$2s2p^3(^3D)3d$	${}^4G_{7/2}$	$2s2p^4$	${}^2D_{5/2}$
27	67.418 ± 0.020	3.53 ± 0.41	67.408	0.010	Si VIII	67.479	-0.061	Si VIII	$2s2p^3(^3D)3d$	${}^2G_{7/2}$	$2s2p^4$	${}^4P_{5/2}$
28a	68.294 ± 0.048	5.20 ± 3.01	68.148	0.146	Si VII	68.148	0.146	Si VII	$2s^22p^3(^4S)3d$	5D_3	$2s^22p^4$	3P_1
28b	68.863 ± 0.016	5.75 ± 0.47	68.715	0.148	Si VII				$2s^22p^3(^2P)3d$	3P_1	$2s^22p^4$	3P_0
29	69.734 ± 0.007	15.37 ± 0.48	69.663	0.071	Si VII	69.664	0.070	Si VII	$2s^22p^3(^2D)3d$	3F_2	$2s^22p^4$	3P_2
30a	70.129 ± 0.009	19.06 ± 0.90	70.027	0.102	Si VII	70.072	0.057	Si VII	$2s^22p^3(^2P)3d$	3F_3	$2s^22p^4$	1D_2
30b			70.072	0.057	Si VII				$2s^22p^3(^2P)3d$	1F_3	$2s^22p^4$	1D_2
31a	70.422 ± 0.016	11.28 ± 0.85	70.222	0.200	Si VII	70.185	0.237	Si VII	$2s^22p^3(^2D)3d$	3D_2	$2s^22p^4$	3P_1
31b			70.250	0.172	Si VII				$2s^22p^3(^2P)3d$	1P_1	$2s^22p^4$	1D_2
32	71.168 ± 0.056	3.28 ± 1.06	71.181	-0.013	Si VI	71.181	-0.013	Si VI	$2s^22p^4(^3P)4d$	${}^2D_{5/2}$	$2s^22p^5$	${}^2P_{3/2}$
33	71.425 ± 0.012	13.93 ± 1.16	71.384	0.041	Si VII	71.384	0.041	Si VII	$2s^22p^3(^2D)3d$	3G_3	$2s^22p^4$	1D_2
34a	71.953 ± 0.008	9.57 ± 0.40	71.900	0.053	Si VI	71.842	0.111	Si VII	$2s^22p^3(^2D)3d$	3P_1	$2s^22p^4$	1D_2
34b			71.955	-0.002	Si VI	71.955	-0.002	Si VII	$2s^22p^3(^2D)3d$	1D_2	$2s^22p^4$	1D_2
35	72.389 ± 0.010	7.24 ± 0.39	72.324	0.065	Si VII	72.324	0.065	Si VII	$2s^22p^3(^2D)3d$	3D_1	$2s^22p^4$	1D_2
36	73.136 ± 0.004	7.50 ± 0.23	73.123	0.013	Si VII	73.123	0.013	Si VII	$2s^22p^3(^2D)3d$	3D_3	$2s^22p^4$	3P_2
37	73.394 ± 0.004	7.44 ± 0.22	73.350	0.044	Si VII	73.311	0.083	Si VII	$2s^22p^3(^2D)3d$	3P_2	$2s^22p^4$	3P_1
38a	75.160 ± 0.038	8.48 ± 0.33	75.193	-0.033	Si VII	75.335	-0.175	Si VII	$2s2p^4(^2P)3d$	1F_3	$2s2p^5$	3P_2

Table 1—Continued

Index	λ_{Exp} Å	Intensity Arb. Unit	λ_{Kelly} Å	$\Delta\lambda$ Å	Ion	$\lambda_{\text{Pres.}}$ Å	$\Delta\lambda$ Å	Ion	Transition		
									Upper	Lower	
38b	75.352±0.042	3.87 ±0.34	75.398	-0.046	Si VI						
39	77.348±0.006	4.43 ±0.20	77.429	-0.081	Si VI	77.429	-0.081	Si VI	$2s^22p^4(^1S)3d$	$^2D_{5/2}$	$2s^22p^5$
40	77.626±0.007	3.74 ±0.20	77.718	-0.092	Si VI	77.718	-0.092	Si VI	$2s^22p^4(^1S)3d$	$^2D_{3/2}$	$2s^22p^5$
41	79.132±0.030	3.26 ±0.58	79.236	-0.104	Si VII	79.237	-0.105	Si VII	$2s^22p^3(^4S)3s$	5S_2	$2s^22p^4$
42	79.448±0.035	2.73 ±0.58	79.491	-0.043	Si VII	79.444	0.004	Si VII	$2s^22p^3(^4S)3s$	5S_2	$2s^22p^4$
43	80.353±0.006	23.54±1.03	80.449	-0.096	Si VI	80.449	-0.096	Si VI	$2s^22p^4(^3P)3d$	$^4D_{5/2}$	$2s^22p^5$
44	80.622±0.013	17.86±0.83	80.725	-0.103	Si VI	80.725	-0.103	Si VI	$2s^22p^4(^3P)3d$	$^4P_{3/2}$	$2s^22p^5$
45	81.382±0.010	11.75±0.60	81.620	-0.238	Si VII	81.617	-0.235	Si VII	$2s^22p^3(^2D)3s$	3D_3	$2s^22p^4$
46	81.698±0.014	7.05 ±0.61	81.895	-0.197	Si VII	81.845	-0.147	Si VII	$2s^22p^3(^2D)3s$	3D_2	$2s^22p^4$
47	82.961±0.003	26.43±0.55	83.128	-0.167	Si VI	83.128	-0.167	Si VI	$2s^22p^4(^3P)3d$	$^2D_{5/2}$	$2s^22p^5$
48a	83.328±0.005	17.19±0.52	83.611	-0.283	Si VI	83.611	-0.283	Si VI	$2s^22p^4(^1D)3d$	$^2D_{3/2}$	$2s^22p^5$
48b			83.526	-0.298	Si VI				$2s^22p^4(^3P)3d$	$^4P_{5/2}$	$2s^22p^5$
49a	83.809±0.007	10.46±0.48	84.082	-0.273	Si VI				$2s^22p^4(^3P)3d$	$^4F_{3/2}$	$2s^22p^5$
49b			84.082	-0.273	Si VII	84.071	-0.262	Si VII	$2s^22p^3(^2D)3s$	1D_2	$2s^22p^4$
50	84.935±0.002	13.08±0.26	85.219	-0.284	Si VII				$2s^22p^3(^2P)3s$	1P_1	$2s^22p^4$
51	85.330±0.004	10.68±0.30	85.584	-0.254	Si VII				$2s^22p^3(^4S)3s$	3S_1	$2s^22p^4$
52	87.629±0.004	7.42 ±0.26	88.008	-0.379	Si VII	87.641	-0.012	Si VII	$2s2p^4(^4P)3s$	3P_2	$2s2p^5$
53	87.934±0.004	9.20 ±0.27	88.330	-0.396	Si XII(2)				$2s^23d$	$^2D_{5/2}$	$2s^22p$
											$^2P_{3/2}$